Supplement of Atmos. Chem. Phys., 26, 4711–4725, 2026
https://doi.org/10.5194/acp-26-4711-2026-supplement

Atmospheric Chemistry and Physics
Open Access
EGU

Supplement of

Rapid formation of secondary aerosol precursors from the autoxidation of C_5–C_8 n-aldehydes

Shawon Barua et al.

Correspondence to: Shawon Barua (shawon.barua@tuni.fi) and Matti Rissanen (matti.rissanen@tuni.fi)

S1. Flow reactor setup and mass spectrometry

A schematic of the flow reactor setup used in *n*-aldehyde OH oxidation reactions is shown in Figure S1. All the reactant gas supply lines were connected to the reactor via PTFE tubing and Swagelok fittings. The gas flows were controlled by Alicat mass flow controllers (MFC). The mass spectrometer chemical ionization inlet flow (8–10 slpm) and the volume of the reactor defines the reaction time of the gas mixture inside the reactor. A 100 cm long borosilicate flow reactor with 4.7 cm inner diameter (i.d.) was used for long reaction time experiments while a quartz flow reactor (length: 100 cm, and i.d.: 2.2 cm) was used for the short reaction time experiments. Short reaction time experiments were achieved by providing the precursor VOC flow via a movable injector tube within the reactor and adjusting the distance of the injector tip with respect to the mass spectrometer orifice. The deuterated water (D_2O) line and the NO line were connected separately only during the hydrogen to deuterium (H/D) exchange experiment and the oxidation experiment in presence of NO, respectively.

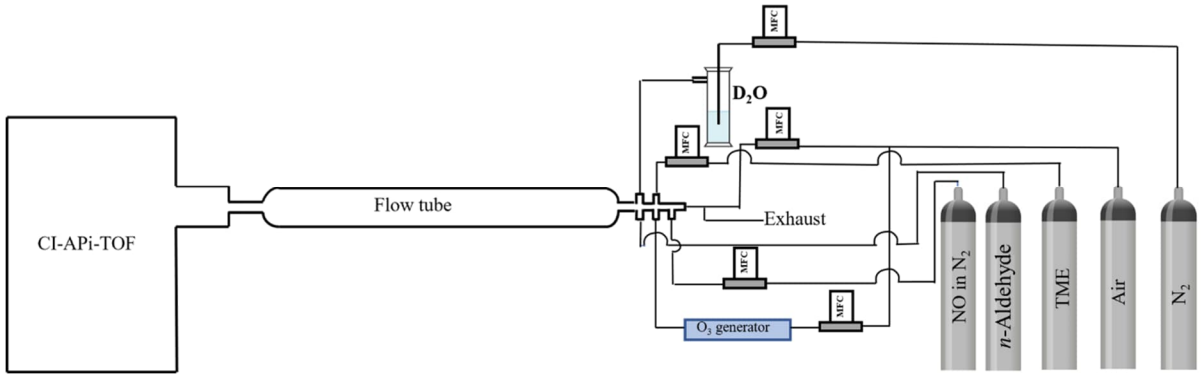

Figure S1. A nitrate (NO_3^-) based chemical ionization mass spectrometer coupled to ambient pressure flow reactor. TME = tetramethylethylene (C_6H_{12}). The oxidant OH radical was produced in situ by TME + O_3 reaction. MFC = mass flow controller. CI-APi-TOF = chemical ionization atmospheric pressure interface time-of-flight mass spectrometer.

The initial concentrations of VOC, TME, and NO in the gas stream were calculated by using equation:

$$[X] = \frac{measured\ flow_x}{measured\ flow_t} \times [MR]$$

where species X can be a VOC, TME, or NO. Here, $measured\ flow_x$ and $measured\ flow_t$ denote the measured flow of the species X and the measured total flow of the gas stream, respectively, while MR is the mixing ratio of the species X in the gas cylinder. On the other hand, the time profiles of VOC, O_3, NO, etc. were estimated from kinetic simulation model

discussed in Section S13 below. The average concentrations of OH, and initial RO_2 radicals under different reaction conditions are given in Table S1.

The mass spectrometric data processing, including averaging, mass axis calibration, and peak integration were done using the tofTools v6.03 package for MATLAB. The signal intensities of all the detected species were normalized using the following expression:

$$S = \frac{[X * NO_3^-]}{[NO_3^-] + [HNO_3NO_3^-] + [(HNO_3)_2NO_3^-]}$$

where $[X * NO_3^-]$ represents the intensity of an individual species X as NO_3^- adduct. In the denominator, $[NO_3^-]$, $[HNO_3NO_3^-]$, and $[(HNO_3)_2NO_3^-]$ represent the intensities of reagent ion monomer, dimer, and trimer, respectively.

We determined the calibration coefficient for our nitrate chemical ionization mass spectrometer (NO_3^--CIMS) to be 2.0×10^9 molecule/cm^3/ncps by calibrating the instrument for sulfuric acid using the method shown by Kürten et al. (2012). A detection limit (LOD) of 2.82×10^3 molecules/cm^3 for sulfuric acid was determined using the equation below.

$$LOD = \frac{3.3 \times \sigma}{S}$$

Here, S is the slope of the calibration curve and σ is the standard deviation of the responses of blank measurements. The HOMs were quantified based on the assumption that they are charged as efficiently as sulfuric acid. The concentrations of the oxidation products including HOMs were calculated by multiplying the individual normalized product signals with the calibration coefficient. The same calibration coefficient was commonly used for all oxidation products because of lack of methods that can account for differences in sensitivity across various oxygenated products. Then, the yields of the products were estimated by dividing their concentrations with the concentration of consumed precursor VOC (i.e., Y_{HOM} = ΔHOM/ΔVOC). Also, note that the flow reactor system exhibits unavoidable wall loss of reactive and condensable species, which contributes to the overall uncertainty in the experimental yields. The normal uncertainty range with the measurement technique has been assumed as asymmetric -50% to +100% (about a factor of two).

S2. Chemicals

High purity Nitrogen gas (5.0 grade) was obtained from Woikoski and Linde Oy. The NO gas cylinder (100 ppm in N_2) was obtained from Air Products. Deuterium oxide (99.9 atom % D)

was obtained from Sigma Aldrich and was transferred to the flow reactor by bubbling nitrogen gas through a liquid D_2O reservoir. The following chemicals were used to make individual gas cylinders diluted in N_2: Tetramethylethylene (98%), hexanal (98%), heptanal (Supelco, purity ≥ 97.0%), and octanal (99%) all from Sigma Aldrich while pentanal (97%) was obtained from Acros Organics. All the chemicals were used without further purification.

S3. *n*-Heptanal ozonolysis background

In the OH initiated oxidation experiment of *n*-heptanal, we used exceptionally low precursor concentrations compared to other studied *n*-aldehydes (see Table 1 in the main manuscript). This was done to reduce the *n*-heptanal ozonolysis background signals originating from unknown contaminants from the heptanal cylinder. The ozonolysis background signals with high and low precursor conditions are shown in Figure S2. Under low precursor condition, we avoid the interference of these background signals with the heptanal OH oxidation products. Figure S2 clearly shows that the heptanal ozonolysis background signals are distinct from the heptanal OH oxidation product signals, $C_7H_{12}O_4$ (m/z 222), $C_7H_{12-14}O_5$ (m/z 238–240), $C_7H_{12-14}O_6$ (m/z 254–256), $C_7H_{12-14}O_7$ (m/z 270–272), $C_7H_{12-14}O_8$ (m/z 286–288), $C_{14}H_{26}O_9$ (m/z 400), $C_{14}H_{26}O_{10}$ (m/z 416), and $C_{14}H_{26}O_{11}$ (m/z 432) that are shown in Figure 3 in the main manuscript.

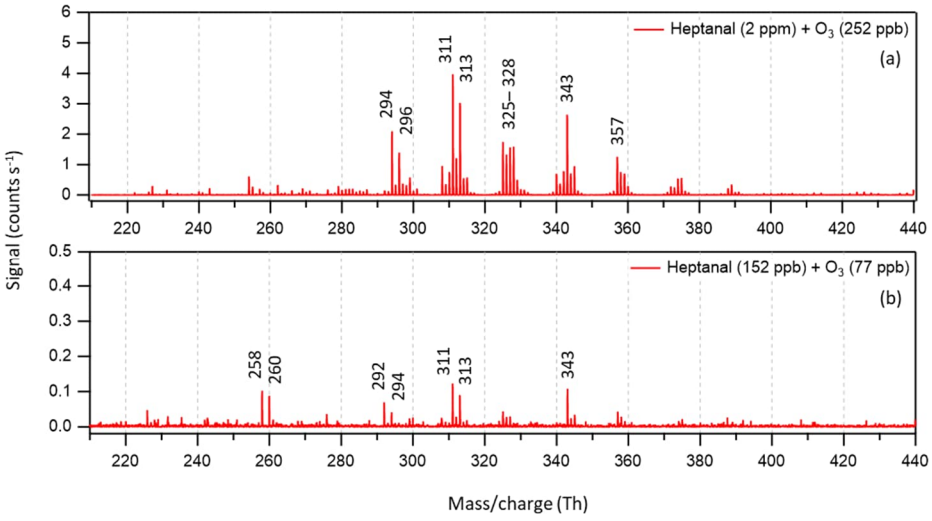

Figure S2. Heptanal + ozone background spectra measured with different reactant concentrations: high (a), and low (b). The unidentified products likely originate from a heptanal stabilizer added by the chemical supplier. Note: Heptanal oxidation experiment initiated by OH radicals (see Figure 3 in the main manuscript) was conducted using the same concentrations of heptanal and ozone as condition (b) and with the addition of TME (as the source of OH).

S4. TME ozonolysis and aldehyde background spectra

To ensure that the *n*-aldehyde + OH oxidation products shown in Figures 2, 3, 5, and 7 of the main manuscript are either distinct or significantly bigger than any background signals, we record all the possible background spectra separately. Figure S3 clearly shows that there are some persistent background signals with nominal mass/charge 226 (panels b–c), 276 (panels b–c), 283 (panel a), 292 (panels a–d), 412 (panels c–d), 440 (panels a and d), etc. present. While most of them are distinct from the nominal mass/charge ratios of the products signals in *n*-aldehyde oxidation, a few of them match with the oxidation products (e.g., m/z 226 with $C_5H_8O_6$ and $C_6H_{12}O_5$, m/z 342 with $C_{11}H_{20}O_8$, and m/z 412 with $C_{16}H_{30}O_8$). Therefore, the backgrounds of TME ozonolysis (TME + O_3) and relevant aldehyde are subtracted from the spectra reported in the main manuscript (Figures 2, 3, and 7) for clarity and thus it ensures that the reported product signals are produced exclusively during the oxidation of *n*-aldehydes.

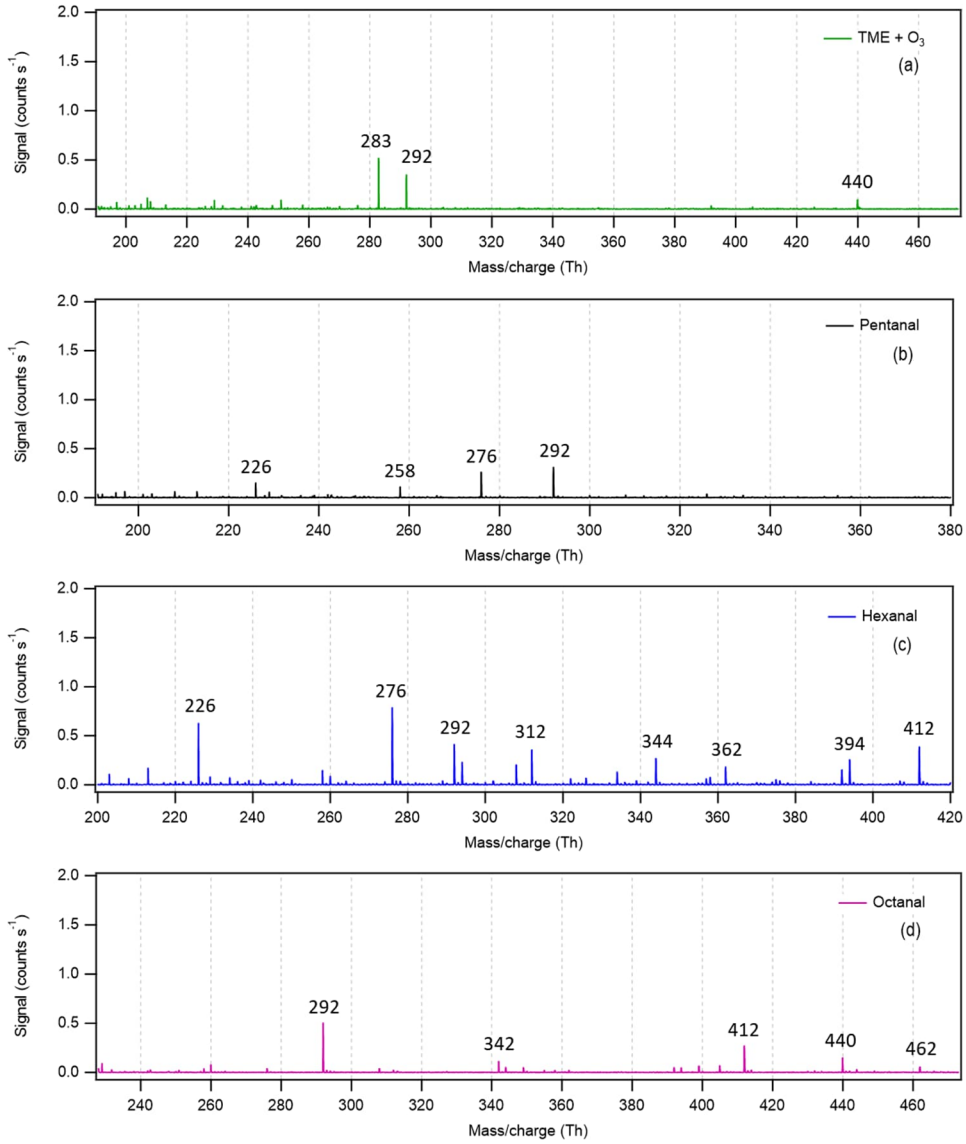

Figure S3: Individual background spectra of TME + O_3 (a), pentanal (b), hexanal (c), and octanal (d) recorded during *n*-aldehyde OH oxidation experiments. The reaction of TME + O_3 is the source of the oxidant OH.

S5. Instrument's responses to changes in reactant flows

The mass spectrometer that used for detecting the oxidation products in different *n*-aldehyde experiments is very sensitive to the changes in reactant gas flow conditions. Figure S4 shows one minute average time series of several product signals that show responses of the detected signals increasing or decreasing depending on how the reactant gas flows are controlled. In Figure S4A, we can see that the reagent ion dimer $HNO_3NO_3^-$ drops immediately with the introduction of D_2O in the flow reactor and raises back with the withdrawal of the D_2O flow. The opposite trend is seen with the corresponding deuterated reagent dimer ion signal $DNO_3NO_3^-$. The product signal of $C_6H_{10}O_6$ gets exchanged with two D atoms and the corresponding $C_6H_8D_2O_6$ shows a similar trend as shown in the bottom part of Figure S4A. When the precursor VOC (hexanal) flow is set to zero, the signal of $C_6H_{10}O_6$ gets dropped completely. In Figure S4B, we can see how the octanal derived dominant $C_8H_{15}O_6$ radical signal responds with various NO flows. It shows a general decreasing trend with the increase of NO concentrations. On the other hand, the corresponding organonitrate $C_8H_{15}O_6NO$ signal raises with up to 200 ppb of NO and then drops with higher NO concentrations.

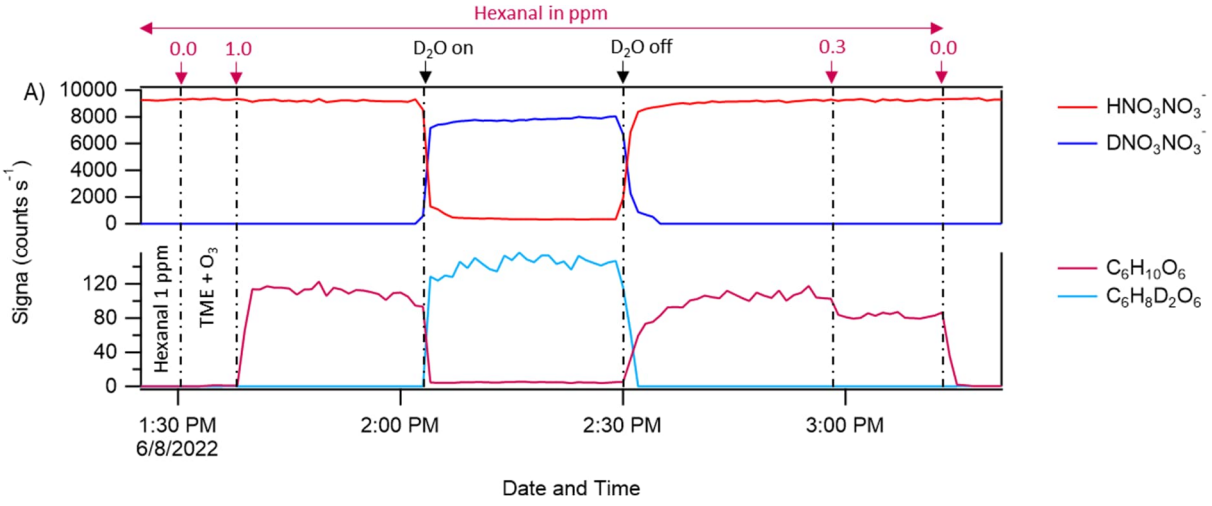

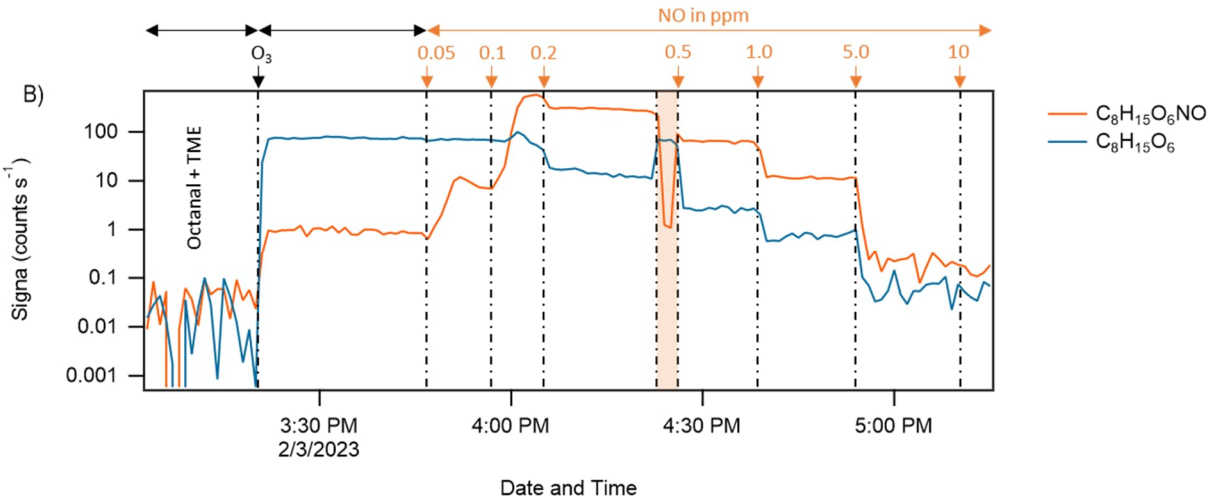

Figure S4. Time series of detected product signals with the changes in different reactant gas flows in OH initiated oxidation of hexanal (A) and octanal (B). The product signals are labelled with the exclusion of NO_3^- ion attachment in their compositions. Panel (A) shows that with the introduction of D_2O in the reaction mixture, labile H atoms in the reagent ion (top part) and in the oxidation product (bottom part) are exchanged with D atoms and the corresponding signals drop and raise accordingly. Panel (B) shows the responses of dominant $C_8H_{15}O_6$ radical and corresponding organonitrate $C_8H_{15}O_6NO$ with various NO flows. The shaded area in panel (B) indicates switching of NO mass flow controllers from smaller range to higher range.

S6. Autoxidation an aldehyde – hexanal

The oxidation reaction of an aldehyde by OH radical is initiated predominantly by the abstraction of the aldehydic hydrogen on C1. The H abstraction can also take place on other carbons (e.g., C4) distant from the aldehydic moiety (see Figure S5 below adapted from Barua et al. (2023)). Both reaction channels produce a carbon centred radical that can add molecular oxygen atoms and form acyl (or alkyl) peroxy radicals ($RC(O)O_2$ or RO_2) which can subsequently autoxidize to form highly oxygenated organic molecules (HOMs). Figure S5 shows that the autoxidation of hexanal along C1 and C4 channels with initial branching of 86% and 8%, respectively, produce the same O_5 RO_2 (A61) as the dominant reaction intermediate. The A61 radical slowly turns over to O_7 RO_2 (A61a) via subsequent reactions along the autoxidation path. The other *n*-aldehydes (e.g., pentanal–octanal) are likely to undergo similar autoxidation mechanism and form HOMs we observed experimentally as shown in the main manuscript.

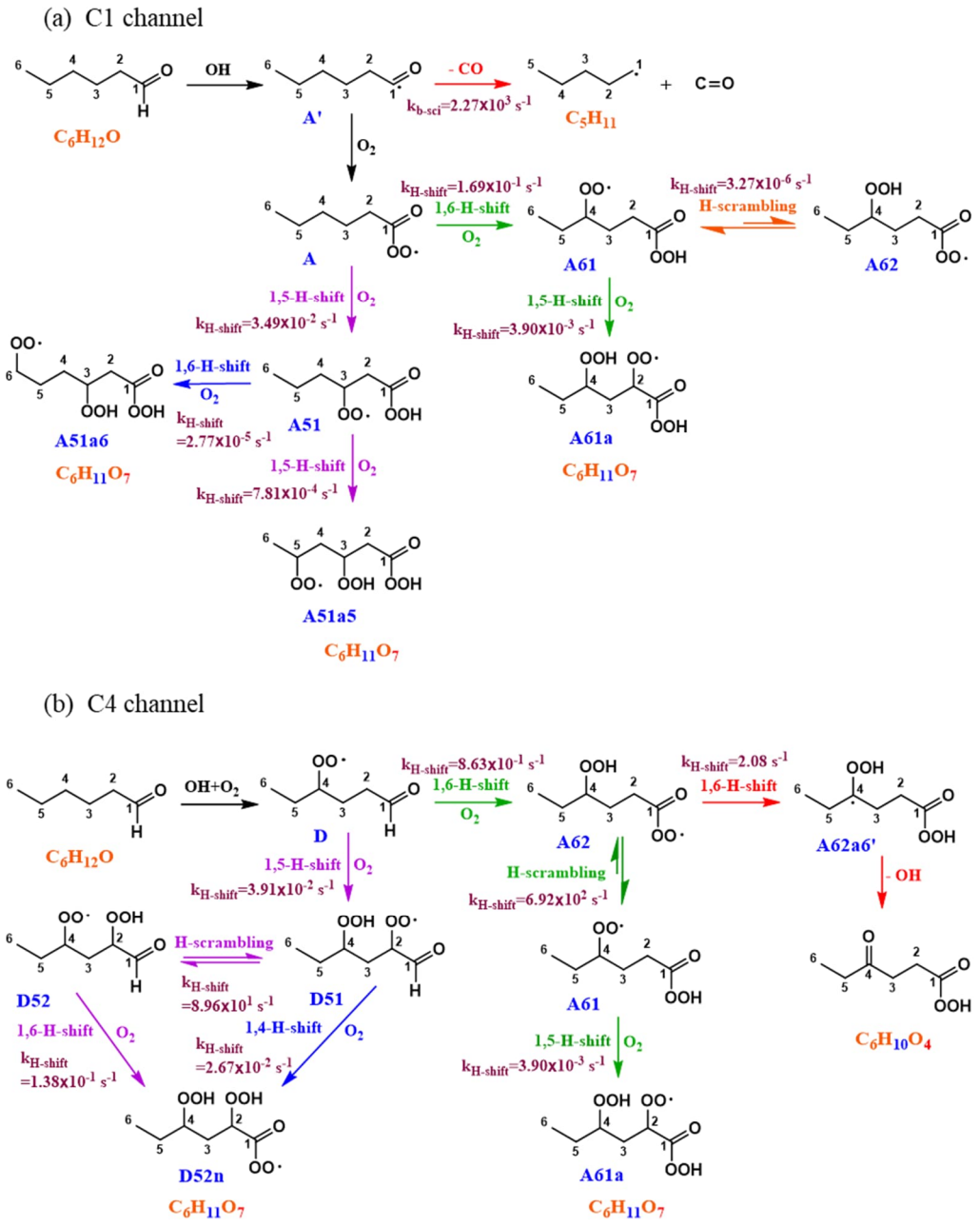

Figure S5. Autoxidation mechanism of hexanal + OH reaction initiated by H atom abstraction from the aldehydic carbon (a) and from a non-aldehydic carbon (b) forming O_7 HOM shown by Barua et al. (2023). Along the dominant aldehydic H abstraction channel (branching ratio 86%), the formation of O_5 product (A61) is very fast and the subsequent H-shift reaction is relatively slower. The non-aldehydic H abstraction channel (branching ratio 8%) shows a slower production of O_5 product (D52) compared to A61, which subsequently undergoes a fast H-shift reaction.

S7. Autoxidation forming O_9 HOM in *n*-aldehydes

With the increase of carbon chain length in the studied *n*-aldehyde oxidation experiments, we observed the formation of more oxygenated products with up to a O_9 monomeric HOM in the case of octanal. In Figure S6, the autoxidation mechanism originated from hexanal work (see Figure S5 above) is extended to HOM up to 9 oxygen atoms. The autoxidation generated radical intermediates ($C_nH_{2n-1}O_{7,9}$) can also undergo chain termination reactions forming closed-shell products via OH loss, via Russell mechanism forming an alcohol and a carbonyl species (red arrows in Figure S6), and H abstraction from HO_2 radicals ($RO_2 + HO_2 \rightarrow ROOH + O_2$).

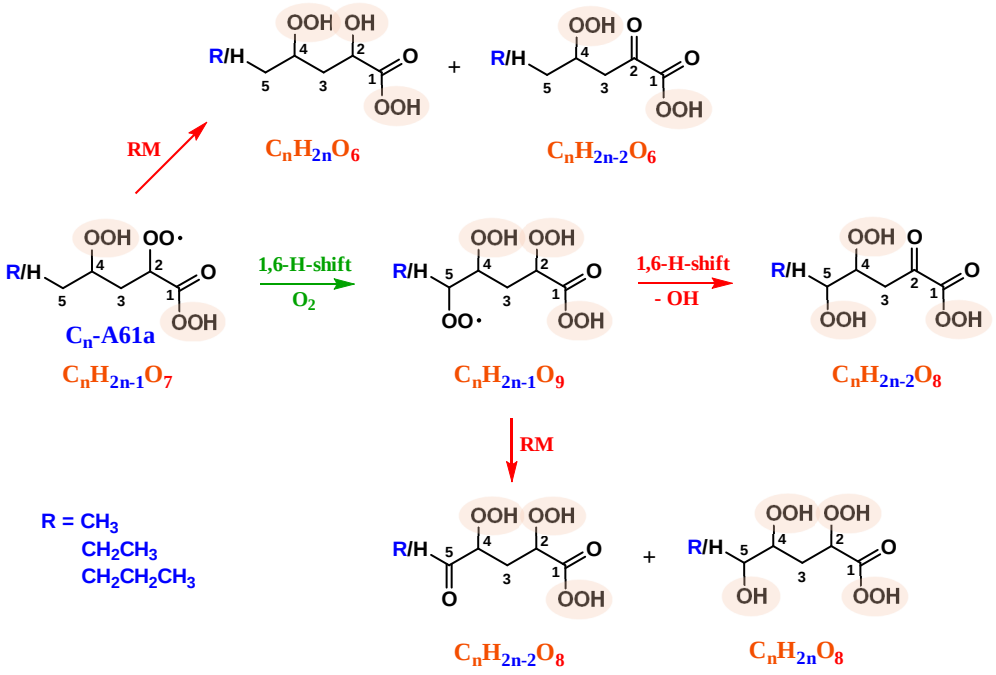

Figure S6. Autoxidation mechanism of *n*-aldehyde + OH reaction extended from Figure S5, showing the formation of HOM up to O_9 (green arrow) along with reaction chain termination products (red arrows). RM = Russell mechanism ($RO_2 + R'O_2 \rightarrow ROH + R'_{-H}C{=}O + O_2$).

S8. Bimolecular reaction products

This section describes potential reaction mechanisms leading to the identified products which involve one RO_2 bimolecular reaction step forming alkoxy radical (RO) intermediates (RO_2 + RO_2 → 2 RO + O_2). While considering H-shift reactions in the alkoxy radicals ($C_nH_{2n-1}O_4$), progressively longer H-shift span (from 1,4 H-shift in $C_5H_9O_4$ to 1,6 H-shift in $C_8H_{15}O_4$, see Figures S7–S10) becomes more relevant (Vereecken and Peeters, 2010) as the carbon chain length of the precursor aldehyde increases. The alkoxy radical can also undergo H-scrambling reaction with the peroxy acid group (Yang et al., 2024) forming hydroxyl acylperoxy radical (see Figure S11 below). These mechanisms show the most probable formation paths of dominant O_6 alkyl peroxy radicals ($C_nH_{2n-1}O_6$) we observed in the studied C_5–C_8 *n*-aldehyde oxidation during short reaction time experiments (see Figure 2 in the main manuscript). In the case of heptanal and octanal in Figures S9–S10, we show the reaction chain propagation forming $C_nH_{2n-1}O_8$ radicals (green arrows) that we observed experimentally (see Figure 3 in the main manuscript). Besides, the likely formation of the closed-shell O_5 and O_6 products originating from $C_nH_{2n-1}O_6$ radicals are also shown in Figures S7–S11. In the molecular structures, the labile hydrogen containing groups are marked in light-brown shapes. The structures associated with the proposed mechanisms are in agreement with the hydrogen to deuterium (H to D) exchange experiments (see Figure 7 in the main manuscript).

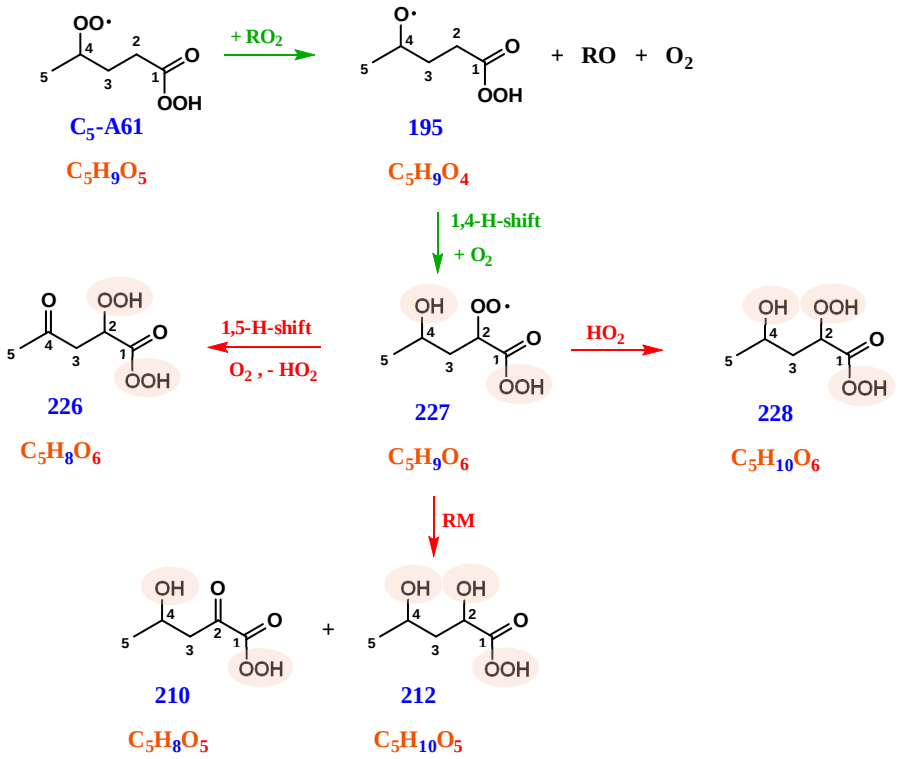

Figure S7. Formation of $C_5H_{8-10}O_6$ products in pentanal + OH reaction likely involve C_5-A61 ($C_5H_9O_5$) peroxy radical undergoing bimolecular reactions with other peroxy radicals (RO_2). The $C_5H_9O_6$ (nominal mass 227) radical likely undergo Russell mechanism (RM: $RO_2 + R'O_2 \rightarrow ROH + R'_{-H}C{=}O + O_2$) forming closed-shell O_5 products.

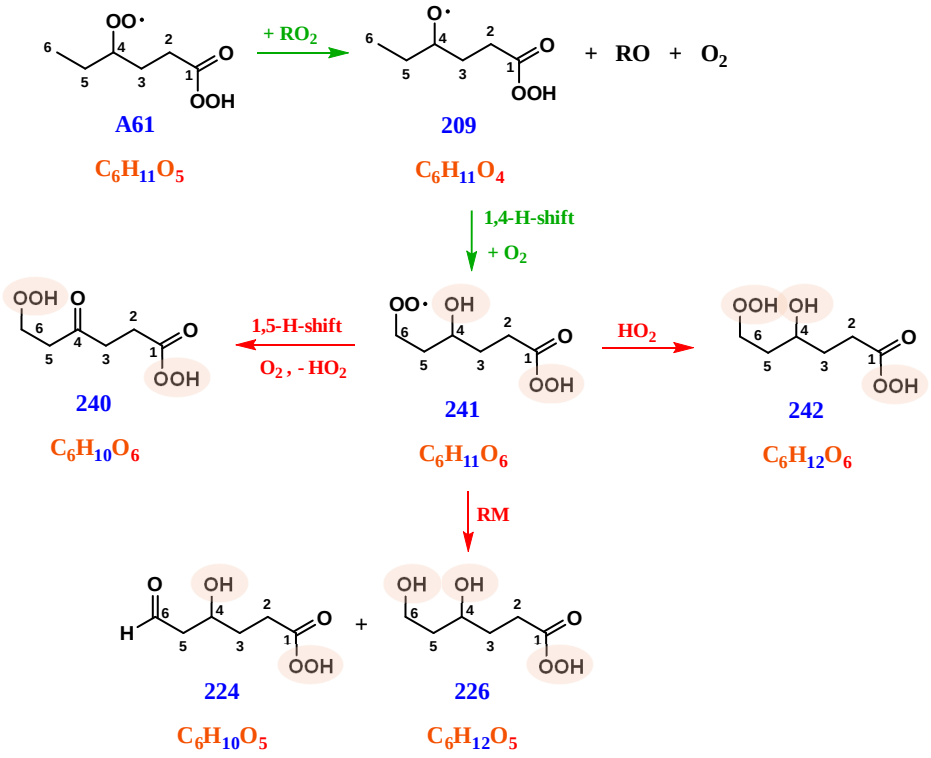

Figure S8. Formation of $C_6H_{10-12}O_6$ products in hexanal + OH reaction likely involve A61 ($C_6H_{11}O_5$) peroxy radical undergoing bimolecular reactions with other peroxy radicals (RO_2). The $C_6H_{11}O_6$ (nominal mass 241) radical likely undergo Russell mechanism (RM: $RO_2 + R'O_2 \rightarrow ROH + R'_{-H}C{=}O + O_2$) forming closed-shell O_5 products.

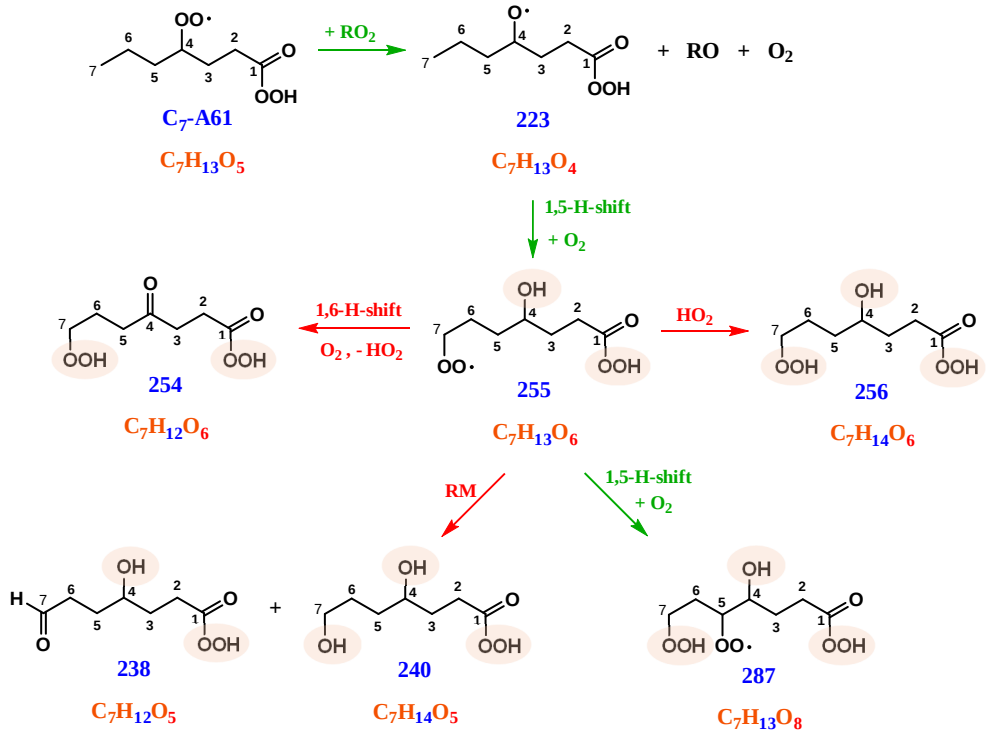

184

185 Figure S9. Formation of $C_7H_{12-14}O_6$ products in heptanal + OH reaction likely involve C_7-A61
186 ($C_7H_{13}O_5$) peroxy radical undergoing bimolecular reactions with other peroxy radicals (RO_2).
187 The $C_7H_{13}O_6$ (nominal mass 255) radical can propagate autoxidation forming $C_7H_{13}O_8$
188 (nominal mass 287) radical (green arrow). It can also undergo Russell mechanism (RM: RO_2
189 + $R'O_2 \rightarrow ROH + R'_{-H}C{=}O + O_2$) forming closed-shell O_5 products.

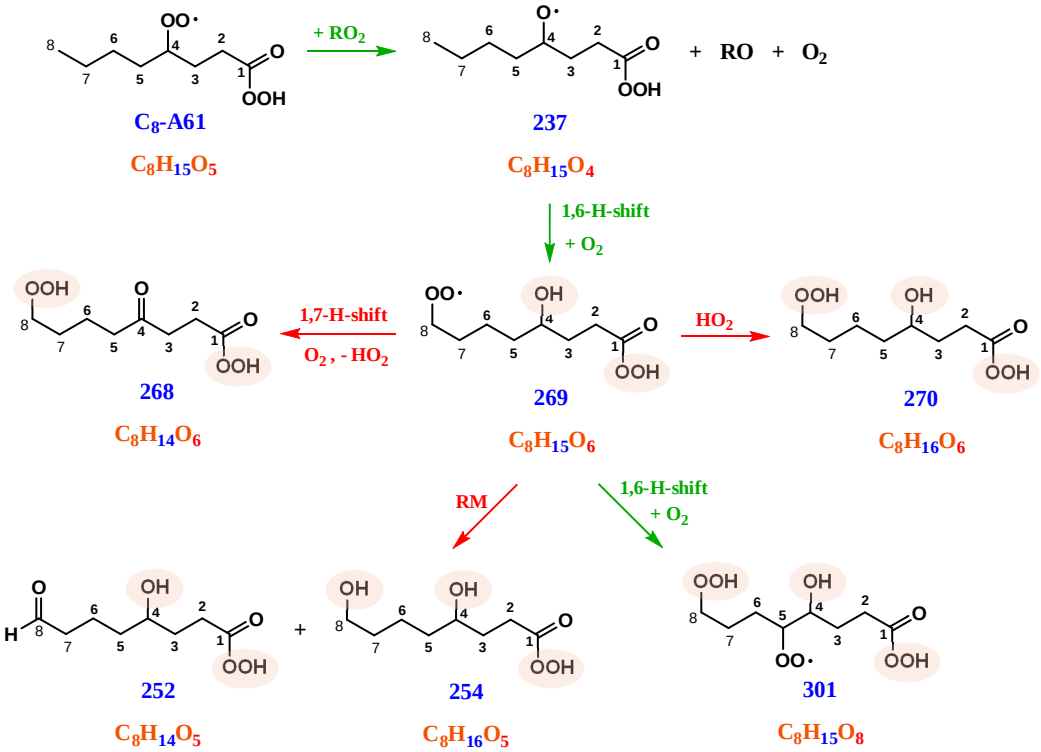

190

Figure S10. Formation of $C_8H_{14-16}O_6$ products in octanal + OH reaction likely involve C_8-A61 ($C_8H_{15}O_5$) peroxy radical undergoing bimolecular reactions with other peroxy radicals (RO_2). The $C_8H_{15}O_6$ (nominal mass 269) radical can propagate autoxidation forming $C_8H_{15}O_8$ (nominal mass 301) radical (green arrow). It can also undergo Russell mechanism (RM: RO_2 + $R'O_2$ → ROH + $R'_{-H}C{=}O$ + O_2) forming closed-shell O_5 products.

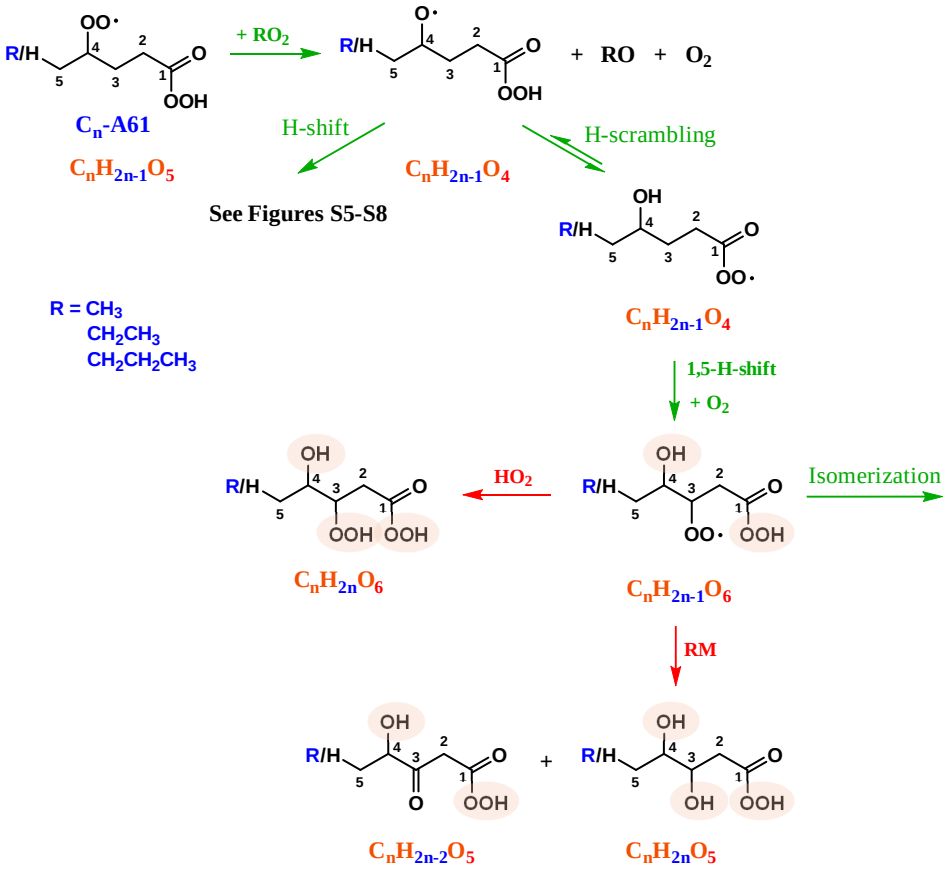

Figure S11. Formation of $C_nH_{2n-1}O_6$ peroxy radical in *n*-aldehyde + OH reaction involving H-scrambling reaction of an alkoxy radical intermediate $C_nH_{2n-1}O_4$ originating from C_n-A61 ($C_nH_{2n-1}O_5$) peroxy radical via bimolecular reactions with other peroxy radicals (RO_2). The O_6 RO_2 radical can propagate autoxidation via isomerization channel (green arrow). It can also react with HO_2 and undergo Russell mechanism (RM: RO_2 + $R'O_2$ → ROH + $R'_{-H}C{=}O$ + O_2) forming closed-shell O_6 and O_5 products, respectively.

S9. HOM accretion products ($C_{2n}H_{4n-2}O_{9-11}$)

In the OH initiated *n*-aldehyde oxidation experiments, we observed the formation of HOM accretion products according to a general reaction RO_2 + $R'O_2$ → ROOR' + O_2 (Hasan et al., 2020; Valiev et al., 2019; Bianchi et al., 2019). The reactions forming the accretion products ($C_{16}H_{30}O_{9-11}$) in octanal oxidation are shown in Figure S12 which involve self and cross

reactions of alkyl peroxy radicals ($C_8H_{15}O_{5-7}$). Note that the molecular structures shown here do not represent their exact spatial orientation but provide the number of available functional groups. In the studied C_5–C_8 *n*-aldehyde systems, the reactant RO_2 radicals ($C_nH_{2n-1}O_{5-7}$) with same number of O atoms have identical number(s) of OH, OOH, and C(O)OOH groups according to Figures S6–S11. The corresponding accretion products ($C_{2n}H_{4n-2}O_{9-11}$) will have an equivalent number of OH, OOH, and C(O)OOH groups as shown here for octanal, marked in light-brown shapes (see Figure S12). These are in agreement with the D_2O mediated H to D shifts (see Figure 7 in the main manuscript).

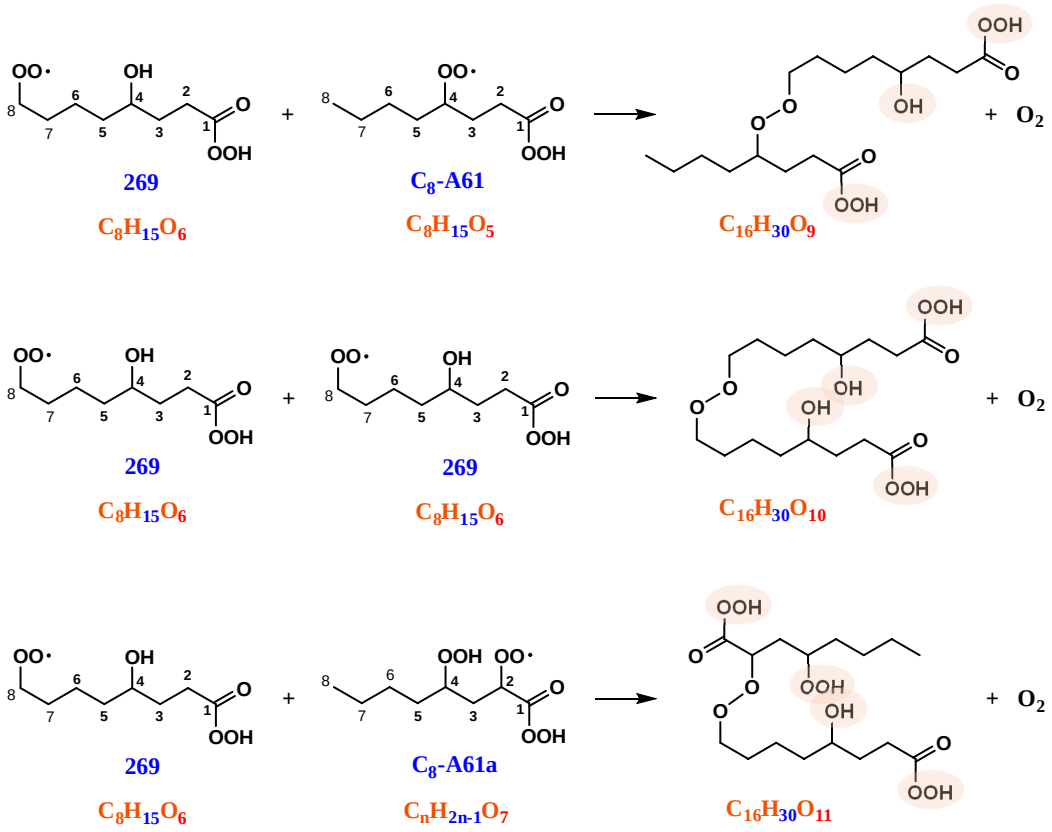

Figure S12. Formation of HOM accretion products ($C_{16}H_{30}O_{9-11}$) in octanal + OH reaction via alkyl peroxy self and cross reactions ($RO_2 + R'O_2 \rightarrow ROOR' + O_2$). Similar reactions apply for other *n*-aldehyde systems involving $C_nH_{2n-1}O_{5-7}$ RO_2 radicals to produce corresponding accretion products ($C_{2n}H_{4n-2}O_{9-11}$) with equivalent number of OH, OOH, and C(O)OOH groups.

S10. TME-derived accretion products

In our *n*-aldehyde oxidation experiments, the oxidant OH radicals were produced in situ by the ozonolysis reaction of tetramethylethylene (TME) (see Figure S13). The reaction leads to the formation of a keto peroxy radical ($C_3H_5O_3$) and acetone (CH_3COCH_3) along with OH radicals. The TME-derived peroxy radical $C_3H_5O_3$ can react with aldehyde-derived peroxy radicals $C_nH_{2n-1}O_{6–8}$ and form different accretion products ($C_{n+3}H_{2n+4}O_{7–9}$) as shown in Figure 3 in the main manuscript. One example of such reactions involving hexanal-derived peroxy radical $C_6H_{11}O_6$ is shown in Figure S13.

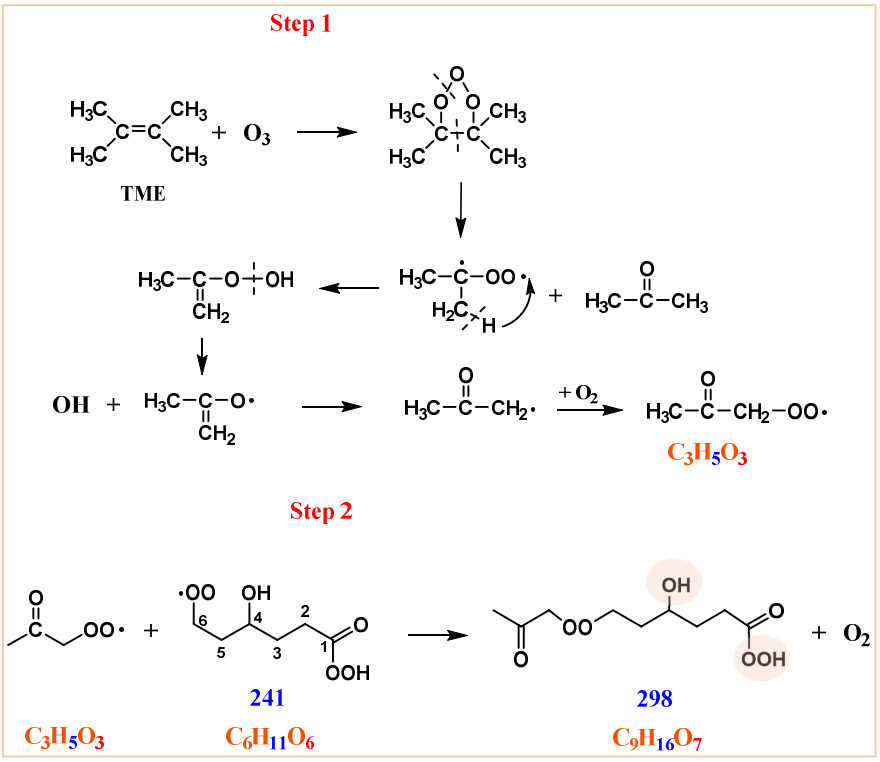

Figure S13. Production of oxidant OH in tetramethylethylene (TME) ozonolysis. The keto peroxy radical $C_3H_5O_3$ is a biproduct and reacts with aldehyde-derived peroxy radicals C_n RO_2 yielding accretion products with C_{n+3} atoms; a pathway producing $C_9H_{16}O_7$ accretion product in hexanal oxidation is shown as an example.

S11. D_2O experiments

During the *n*-aldehyde OH oxidation experiments in presence of D_2O, a near complete H/D exchange was achieved which is most conveniently monitored from the reagent ions, from the shift of $HNO_3NO_3^-$ and $(HNO_3)_2NO_3^-$signals by one and two mass unit, respectively on the mass spectrum (see Figure S14).

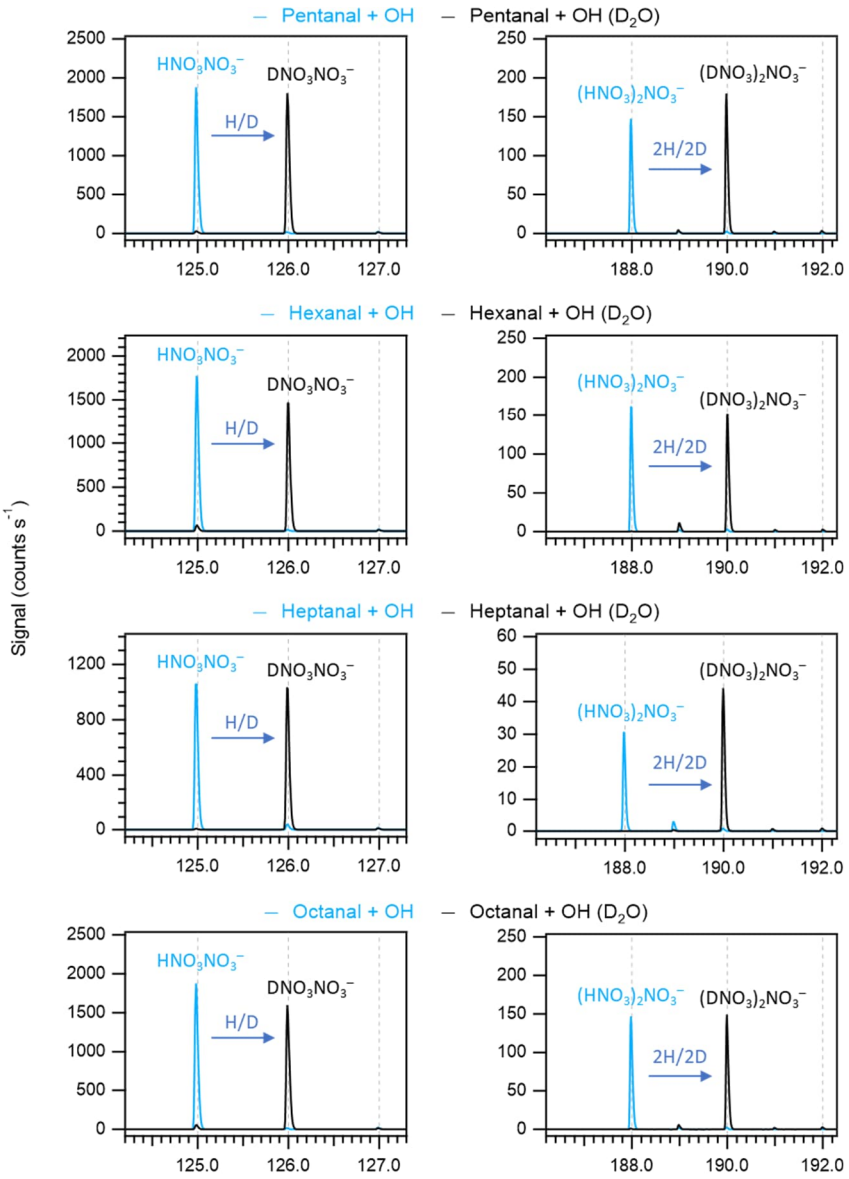

Figure S14. H/D exchange in the reagent ions $HNO_3NO_3^-$ and $(HNO_3)_2NO_3^-$ converting them into $DNO_3NO_3^-$ and $(DNO_3)_2NO_3^-$, respectively, during different *n*-aldehyde OH oxidation reaction in presence of D_2O.

S12. Abundance of HOM in varying NO conditions

This section provides additional insights into the abundance of HOMs in *n*-aldehyde oxidation experiments under varying average NO concentrations. Figure S15A shows that the intensities of closed-shell product signals $C_5H_8O_{4-6}$ somewhat increased at 1 ppb NO condition which then started to decrease under higher NO of ~30 ppb and above in pentanal oxidation. A similar trend was observed with their corresponding yields as shown in Figure 6a in the main manuscript. In both pentanal and hexanal oxidations, the dominant O_6 peroxy radicals ($C_5H_9O_6$

and $C_6H_{11}O_6$ respectively, blue markers) seem to have retained their initial intensities under up to ~30 ppb of average NO (Figure S15 A–B).

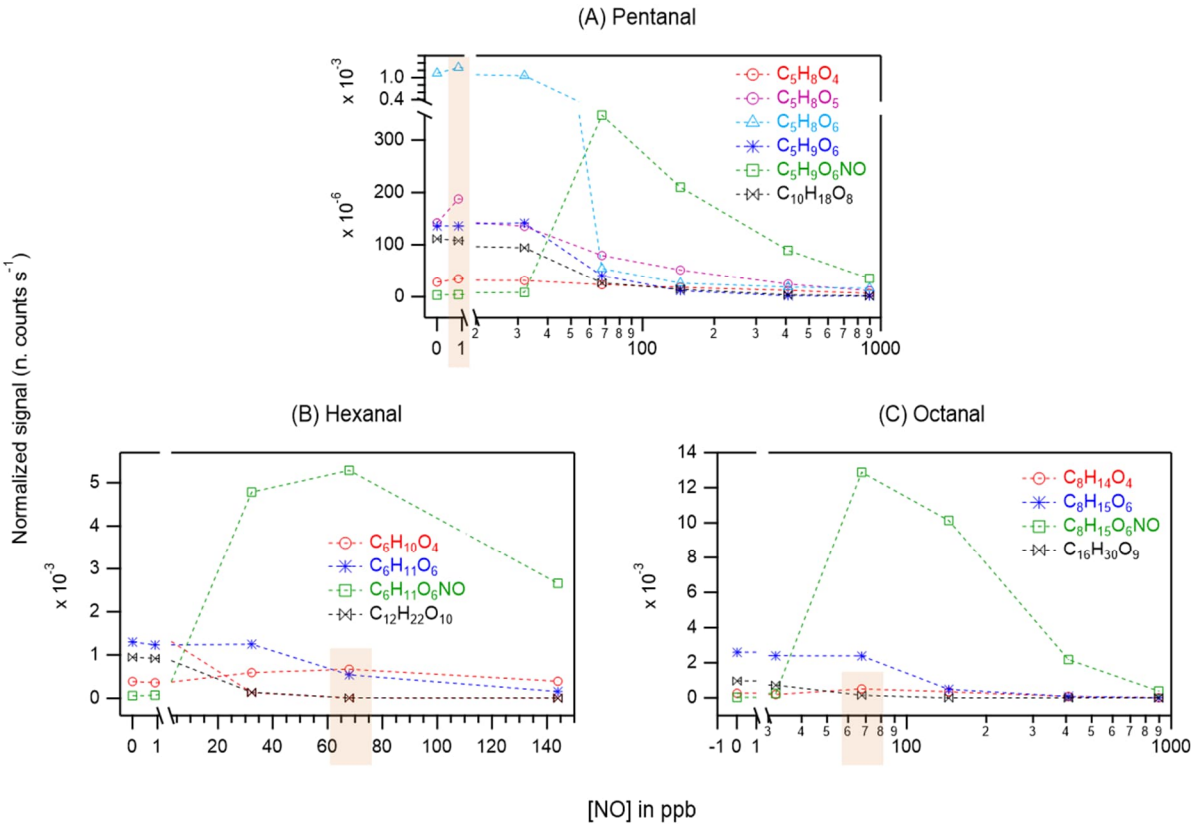

Figure S15. The response (in normalized counts s^{-1}) of different oxidation product signals including monomeric HOMs, organonitrates (green markers), and HOM accretion products (black markers) as a function of average NO concentrations in OH initiated oxidation of *n*-aldehydes: pentanal (A), hexanal (B), and octanal (C). Note the logarithmic scale (x-axis) in panels A and C. The orange rectangles include the enhanced non-nitrogen containing product signals: O_4–O_6 closed-shell products from pentanal at ~1 ppb NO (A), O_4 closed-shell products from hexanal and octanal at ~70 ppb NO (B and C). Reaction time, Δt = 11–13 s.

On the other hand, in octanal oxidation, the dominant O_6 peroxy radical ($C_8H_{15}O_6$) seems to have maintained almost its initial level of signal intensity even under ~70 ppb of NO (see Figure S15C). Interestingly, the corresponding yields of the peroxy radicals increased under those NO conditions (i.e., ~30 ppb average NO for pentanal and hexanal, and up to ~70 ppb NO for octanal; see Figure 6 in the main manuscript) compared to their yields under zero NO condition. Although the abundance of the peroxy radicals did not increase with varying NO conditions, their higher yields were because of the lower consumptions of corresponding precursor aldehydes. Indeed, in the presence of NO, the reaction of the aldehyde with OH competes with

the NO + OH reaction, leading to lower aldehyde consumption (see Figure S17 in Section S13). In all the *n*-aldehydes studied, although the intensities of highly oxygenated products were suppressed under higher NO concentrations, we observed some enhancement in the early oxygenated closed shell products (O_4–O_5, and even O_6 product in pentanal) under relatively lower NO concentrations.

S13. Kinetic simulation

S13.1 Simulations without and with NO

Chemical kinetic simulations were carried out using Kinetiscope Program (Bunker et al., 1974; Gillespie, 1976; Hinsberg and Houle, 2022) to estimate the concentrations of oxidant OH and initial RO_2 radicals in different *n*-aldehyde oxidation reactions without (reaction steps 1–3, 8–10 below) and with the presence of NO (reaction steps 1–12 below). For the reactions of different *n*-aldehydes with OH radical, we used the rate coefficients of 2.66×10^{-11}, 2.85×10^{-11}, and 3.0×10^{-11} cm^3 $molecule^{-1}$ s^{-1} for pentanal (PTL), hexanal (HXL), and octanal (OTL), respectively, reported by Mellouki et al. (2015). In our flow reactor setup, we produced OH radicals in situ by the ozonolysis reaction of tetramethyl ethylene (TME). The produced OH radicals react with TME as well as with the aldehyde in the flow reactor. In the simulations, we used reaction rate coefficients k_{TME-O_3} of 1.5×10^{-15} and k_{TME-OH} of 1.0×10^{-10} cm^3 $molecule^{-1}$ s^{-1} accounting for the reactions of TME with ozone and OH, respectively (Manion et al., 2015). The initial precursor concentrations of aldehyde, TME, ozone, and NO identical to the experimental conditions (see Table S1 below) were used. These include 1.3–2.5 ppm (6.15–3.20×10^{13} molecules cm^{-3}) of pentanal, 1 ppm (2.46×10^{13} molecules cm^{-3}) of hexanal, 0.72 ppm (1.77×10^{13} molecules cm^{-3}) of octanal, 43.2–48.2 ppb (1.06–1.19×10^{12} molecules cm^{-3}) of TME, and 208–295 ppb (5.12–7.26×10^{12} molecules cm^{-3}) of ozone. In the flow reactor experiments, high VOC concentrations were used to scavenge OH, especially as TME reacts so fast with it. Following the reaction of aldehyde with OH, the initially formed carbon centered radical readily undergoes a pseudo unimolecular reaction with O_2 to form the first RO_2 radical. For simplification, we show the formation of different RO_2 radicals directly from the reactions of aldehyde with OH, and TME with OH. Here, TME-produced RO_2 and aldehyde-produced RO_2 are separated by the expressions RO_2_T and RO_2_A, respectively.

With the addition of NO in the reaction system, it is expected to influence the concentrations of OH radicals and initial RO_2 radicals. Therefore, to simulate the experiments with NO, we

included the bimolecular reaction rate coefficients of $k_{NO-OH} = 3.3 \times 10^{-11}$, $k_{HONO-OH} = 6.0 \times 10^{-12}$, $k_{NO-O_3} = 1.8 \times 10^{-14}$, and $k_{NO_2-OH} = 4.1 \times 10^{-11}$ cm^3 $molecule^{-1}$ s^{-1} (Atkinson et al., 2004), with respect to their corresponding reactions in the simulation. In addition, bimolecular rate coefficients for RO_2 + RO_2 and RO_2 + NO reactions were set to the generic values of 3.2×10^{-11} and 9.0×10^{-12} cm^3 $molecule^{-1}$ s^{-1}, respectively (Berndt et al., 2018; Jenkin et al., 2019) to account for sinks of RO_2 radicals. The influences of NO + HO_2, RO_2 + HO_2, and RO_2 + NO_2 reactions on OH and RO_2_A radical concentrations were examined separately and discussed in the section below. An example of the reaction steps used in the current simulation is as follows. The results are shown in Figure S16 and Table S1.

1. TME + O_3 => OH ($k_{TME-O_3} = 1.5 \times 10^{-15}$ cm^3 $molecule^{-1}$ s^{-1})
2. TME + OH => RO_2_T ($k_{TME-OH} = 1.0 \times 10^{-10}$ cm^3 $molecule^{-1}$ s^{-1})
3. OTL + OH => RO_2_A ($k_{OTL-OH} = 3.0 \times 10^{-11}$ cm^3 $molecule^{-1}$ s^{-1})
4. NO + OH => HONO ($k_{NO-OH} = 3.3 \times 10^{-11}$ cm^3 $molecule^{-1}$ s^{-1})
5. HONO + OH => H_2O + NO_2 ($k_{HONO-OH} = 6.0 \times 10^{-12}$ cm^3 $molecule^{-1}$ s^{-1})
6. NO + O_3 => NO_2 + O_2 ($k_{NO-O_3} = 1.8 \times 10^{-14}$ cm^3 $molecule^{-1}$ s^{-1})
7. NO_2 + OH => HNO_3 ($k_{NO_2-OH} = 4.1 \times 10^{-11}$ cm^3 $molecule^{-1}$ s^{-1})
8. 2 RO_2_T => Sink_a ($k_{RO_2-RO_2} = 3.2 \times 10^{-11}$ cm^3 $molecule^{-1}$ s^{-1})
9. 2 RO_2_A => Sink_b ($k_{RO_2-RO_2} = 3.2 \times 10^{-11}$ cm^3 $molecule^{-1}$ s^{-1})
10. RO_2_T + RO_2_A => Sink_ab ($k_{RO_2-RO_2} = 3.2 \times 10^{-11}$ cm^3 $molecule^{-1}$ s^{-1})
11. RO_2_T + NO => $RONO_2$ ($k_{RO_2-NO} = 9.0 \times 10^{-12}$ cm^3 $molecule^{-1}$ s^{-1})
12. RO_2_A + NO => $RONO_2$ ($k_{RO_2-NO} = 9.0 \times 10^{-12}$ cm^3 $molecule^{-1}$ s^{-1})

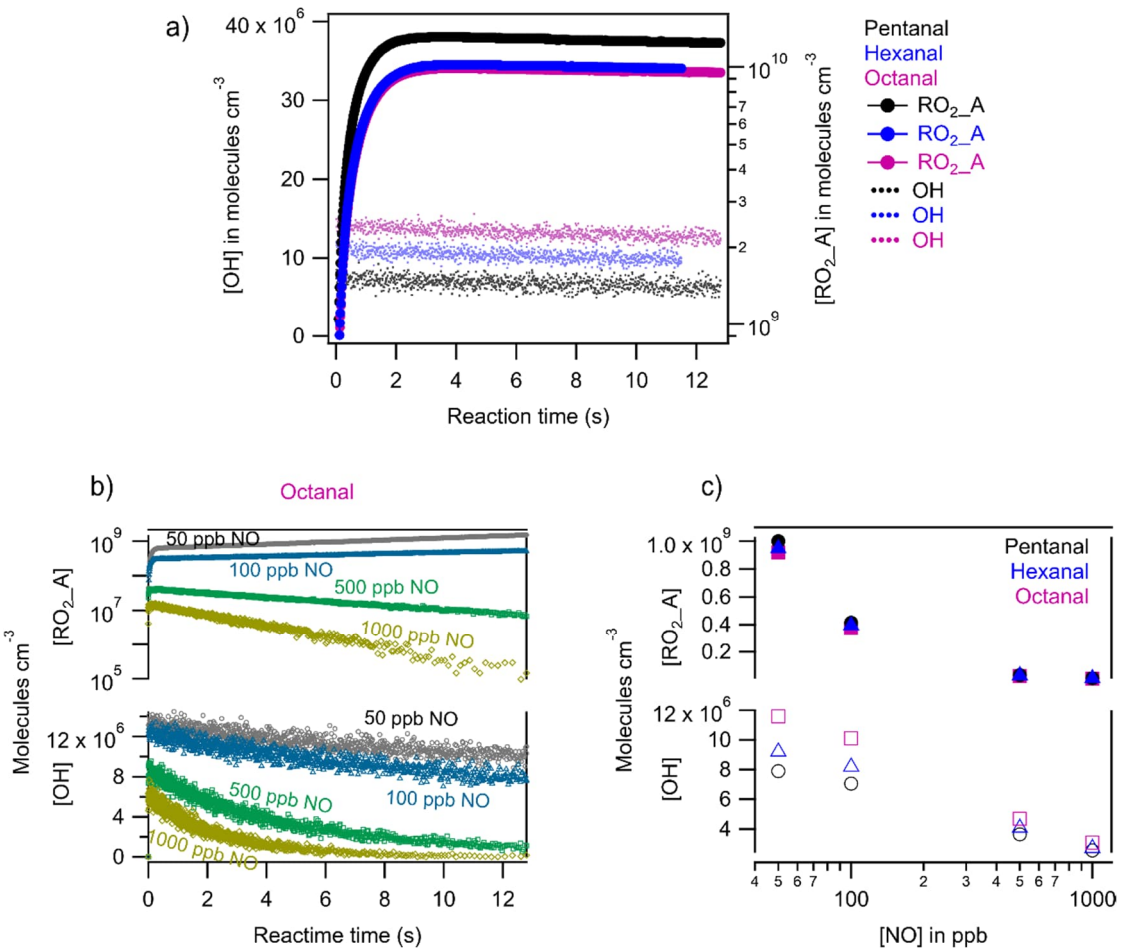

Figure S16. Concentration profiles of OH and initial RO_2_A radicals produced in *n*-aldehyde oxidation derived by chemical kinetic simulations under laboratory flow reactor experimental condition without NO (a) and with NO (b–c). Panel (b) shows results from octanal. In panel (c), average concentrations of OH and RO_2_A radicals during 11–13 s reaction time are presented in open and filled markers, respectively.

Figure S16a and Table S1 imply that the average concentrations of oxidant OH and initial RO_2_A radicals in the flow reactor are comparable in different *n*-aldehyde oxidation experiments. In the experiments without NO, the simulation produced average concentrations of OH radicals are 6.78×10^6, 1.03×10^7, and 1.33×10^7 molecules cm^{-3} for the experiments with PTL, HXL, and OTL, respectively.

Table S1. Average concentrations of OH and initial RO_2 radicals and reacted precursor aldehyde concentrations (ΔVOC) in different *n*-aldehyde oxidation experiments derived from kinetic simulations under laboratory conditions. Reaction time, Δt = 11–13 s.

Expt. type (VOC)	**Model input**				**Model output**		
	[VOC] ppmv	**[TME] ppbv**	**[O_3] ppbv**	**[NO]$_{t=0}$ ppbv**	**Δ[VOC] ppbv**	**[OH] #/cm^3**	**[RO_2_A] #/cm^3**
Simulation without NO							
PTL	2.5	48.2	295	–	5.78	6.78×10^6	1.21×10^{10}
HXL	1.0	43.2	225	–	3.39	1.03×10^7	9.37×10^9
OTL	0.72	48.2	208	–	3.65	1.33×10^7	9.12×10^9
In the presence of NO							
PTL	1.3	48.2	208	0	3.91	8.84×10^6	9.67×10^9
				50	3.42	7.90×10^6	1.00×10^9
				100	2.98	7.06×10^6	4.14×10^8
				500	1.09	3.64×10^6	3.26×10^7
				1000	0.43	2.55×10^6	1.05×10^7
HXL	1.0	43.2	225	50	2.96	9.22×10^6	9.49×10^8
				100	2.58	8.20×10^6	3.96×10^8
				500	0.98	4.09×10^6	3.06×10^7
				1000	0.38	2.72×10^6	9.34×10^6
OTL	0.72	48.2	208	50	3.12	1.16×10^7	9.18×10^8
				100	2.67	1.01×10^7	3.71×10^8
				500	0.88	4.70×10^6	2.64×10^7
				1000	0.33	3.09×10^6	7.98×10^6

The corresponding estimated RO_2_A radical concentrations are 1.21×10^{10}, 9.37×10^9, and 9.12×10^9 molecules cm^{-3}, respectively. While the average OH concentrations for HXL and OTL experiments are closer to each other, it is somewhat lower for the PTL experiment by a factor of 1.5 to 2 despite having higher initial ozone concentration. This can be attributed to the OH radical consumption by higher precursor PTL concentration compared to that of HXL and OTL. It is reflected in the concentrations of initial RO_2_A radicals in the three studied systems which are rather comparable and we aim for this as the starting condition for autoxidation. Note the sequential increase in reaction rate coefficients of aldehydes (from PTL to OTL) with OH radical mentioned above. In the presence of NO, Figure S16b shows how the concentration profiles of OH and RO_2_A radicals evolve in time with OTL oxidation experiment as an example. In all the *n*-aldehyde systems studied, the primary RO_2_A radical concentration steadily increases with time under 50 ppb and 100 ppb initial NO conditions. However, at 500 ppb and 1000 ppb NO conditions, the concentrations of RO_2_A radicals decrease with time soon after achieving their initial peak values. In the case of OH radicals, the

concentrations show a general decreasing trend with time while at higher NO conditions (from 500 ppb initial NO), we observe a faster decreasing tendency in concentrations as expected. It is also rewarding to see that the initial RO_2_A radical concentrations from the studied *n*-aldehydes are comparable under various NO conditions (see Figure S16c and Table S1). Furthermore, it is important to mention that the concentrations of oxidant OH and primary RO_2_A radicals reported here are at their upper limits as the loss of the radicals to the reactor wall is not accounted. Therefore, in our flow reactor experiments, the concentrations of the reactive radical species are close to the expected concentrations in the ambient air, and we believe they are well representative.

Under higher initial NO conditions, OH radical concentrations are depleted predominantly via its reaction with NO (reaction step 4) as well as via the drop of reactant ozone (reaction step 6) concentrations. Figure S17 shows the time series of NO, O_3, and precursor aldehyde concentrations estimated by the simulations. A faster drop of ozone concentrations is seen under higher initial NO concentrations of 500 ppb and above compared to lower NO concentrations (panels a, c and e of Figure S17). This is reflected in the estimated OH concentrations (Figure S16c and Table S1) as well as in the consumption of precursor aldehydes (see panels b, d and f of Figure S17, and ΔVOC in Table S1).

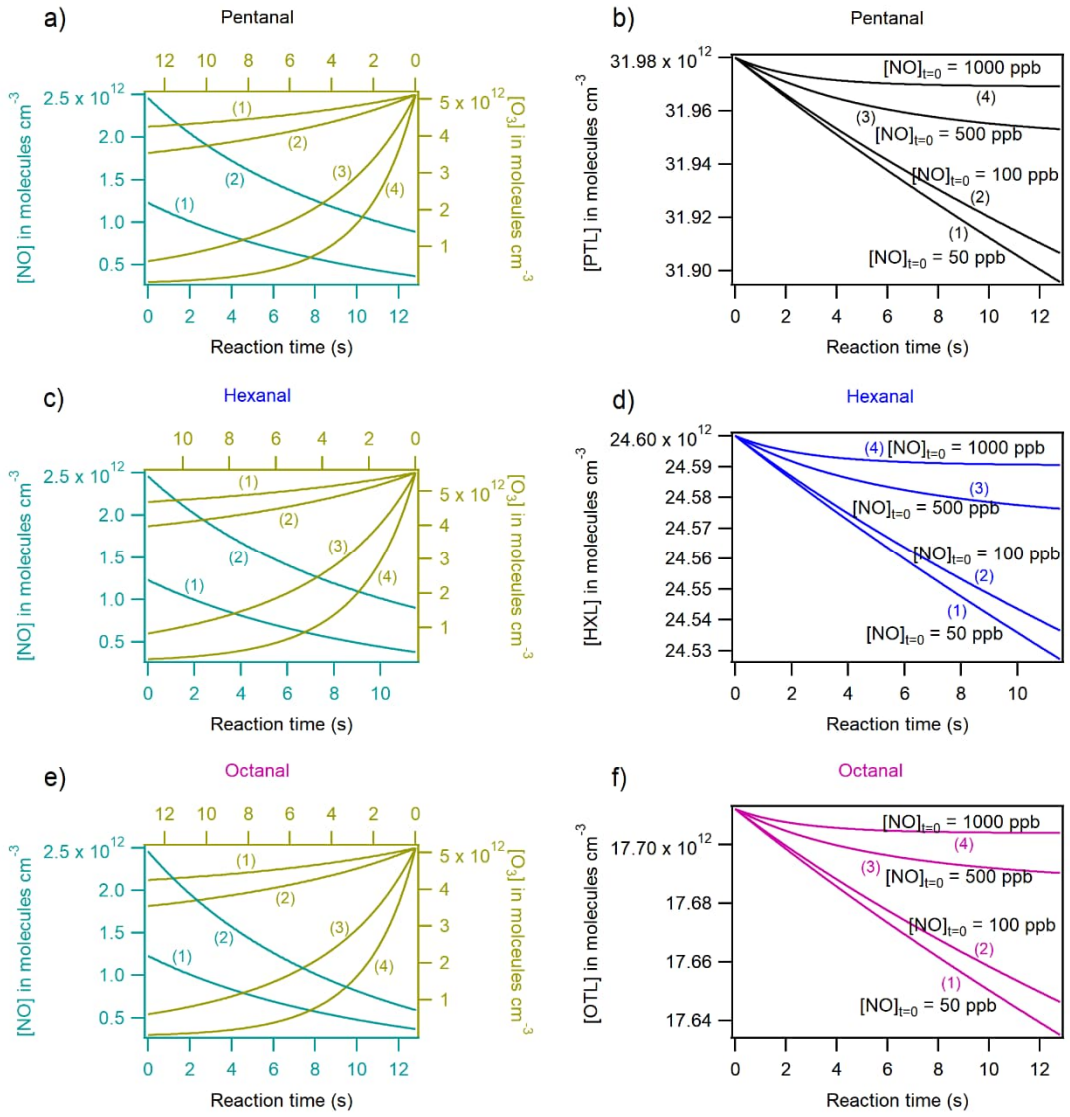

Figure S17. Concentration profiles of NO, O_3, and *n*-aldehyde as a function of reaction time under different initial $[NO]_{t=0}$ conditions: pentanal (a–b), hexanal (c–d), and octanal (e–f). The initial NO conditions are marked with numbers within parenthesis: $[NO]_{t=0}$ = 50 ppb (1), $[NO]_{t=0}$ = 100 ppb (2), $[NO]_{t=0}$ = 500 ppb (3), and $[NO]_{t=0}$ = 1000 ppb (4). Reaction time, Δt = 11–13 s. PTL = pentanal, HXL = hexanal, and OTL = octanal.

S13.2 Impact of HO_2 on OH and RO_2

In the gas-phase oxidation process of volatile organic compounds (VOCs), it is usual to produce hydroperoxy radicals (HO_2) alongside the production of alkyl peroxy radicals (RO_2). In the presence of NO, the HO_2 radicals react with NO to recycle OH and NO_2 radicals in the reaction system (see reaction step 13) (Atkinson et al., 2004). In addition, the reaction of HO_2 with RO_2 can produce closed shell hydroperoxide (ROOH) along with other products (Boyd et al., 2003).

Here, we included these reactions as other sinks of RO_2 in the simulation (reaction steps 14–15).

13. HO_2 + NO => OH + NO_2 (k_{HO_2-NO} = 8.91 × 10^{-12} cm^3 $molecule^{-1}$ s^{-1})

14. RO_2_T + HO_2 => Sink_c ($k_{RO_2-HO_2}$ = 2.2 × 10^{-11} cm^3 $molecule^{-1}$ s^{-1})

15. RO_2_A + HO_2 => Sink_d ($k_{RO_2-HO_2}$ = 2.2 × 10^{-11} cm^3 $molecule^{-1}$ s^{-1})

In the flow reactor system, we presume that the production of HO_2 radicals is about 30% of total RO_2 radicals (RO_2_T + RO_2_A) during the reaction time. Therefore, to examine the influence of the HO_2 reactions with NO and RO_2 on the concentrations of OH and RO_2_A radicals, we ran a separate set of simulations on Kinetiscope including the reaction steps 13–15. An initial HO_2 concentration of 30% of total RO_2 (e.g., 1.35 × 10^8 molecules cm^{-3} of HO_2 in OTL oxidation at 100 ppb initial NO condition) obtained from the previous simulation without HO_2 was used in the subsequent simulation. Figure S18 shows the results of HXL and OTL oxidation processes without and with involving the reaction steps 13–15. In all *n*-aldehyde simulations, the reaction steps 13–15 do not seem to alter the average concentrations of OH and RO_2_A radicals given that the reaction scheme (reaction steps 1–15) is lacking a constant source of 30% HO_2. To examine the maximum possible OH recycling from the reaction step 13, we also conducted another set of simulations by excluding reaction steps 14–15. Again, this approach reproduced the same levels of average OH and RO_2_A concentrations highlighting that the OH radical recycling under the studied NO conditions are not likely significant.

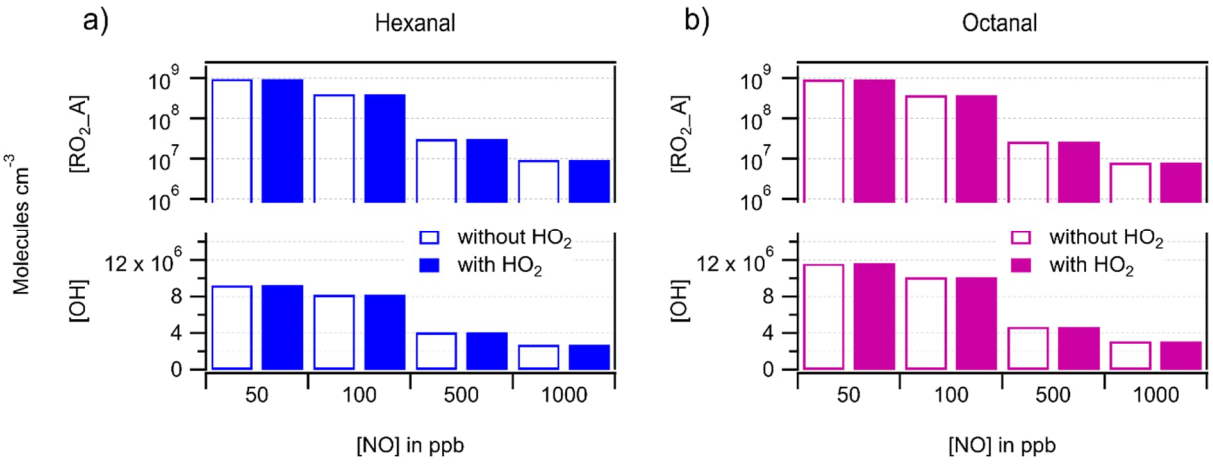

Figure S18. Average concentrations of OH and initial RO_2_A radicals produced in hexanal (a) and octanal (b) oxidation derived by chemical kinetic simulations under laboratory conditions with varying initial NO. Simulations that include the reactions of HO_2 with NO and RO_2

(reaction steps 13–15) are presented in filled bars while simulations without these reaction steps are presented in open bars.

References

Atkinson, R., Baulch, D. L., Cox, R. A., Crowley, J. N., Hampson, R. F., Hynes, R. G., Jenkin, M. E., Rossi, M. J., & Troe, J. (2004). Evaluated kinetic and photochemical data for atmospheric chemistry: Volume I - gas phase reactions of O_x, HO_x, NO_x and SO_x species. *Atmospheric Chemistry and Physics*, *4*(6), 1461–1738. https://doi.org/10.5194/acp-4-1461-2004

Barua, S., Iyer, S., Kumar, A., Seal, P., & Rissanen, M. (2023). An aldehyde as a rapid source of secondary aerosol precursors: Theoretical and experimental study of hexanal autoxidation. *Atmospheric Chemistry and Physics*, *23*(18), 10517–10532. https://doi.org/10.5194/acp-23-10517-2023

Berndt, T., Scholz, W., Mentler, B., Fischer, L., Herrmann, H., Kulmala, M., & Hansel, A. (2018). Accretion Product Formation from Self- and Cross-Reactions of RO_2 Radicals in the Atmosphere. *Angewandte Chemie International Edition*, *57*(14), 3820–3824. https://doi.org/10.1002/anie.201710989

Bianchi, F., Kurtén, T., Riva, M., Mohr, C., Rissanen, M. P., Roldin, P., Berndt, T., Crounse, J. D., Wennberg, P. O., Mentel, T. F., Wildt, J., Junninen, H., Jokinen, T., Kulmala, M., Worsnop, D. R., Thornton, J. A., Donahue, N., Kjaergaard, H. G., & Ehn, M. (2019). Highly Oxygenated Organic Molecules (HOM) from Gas-Phase Autoxidation Involving Peroxy Radicals: A Key Contributor to Atmospheric Aerosol. *Chemical Reviews*, *119*(6), 3472–3509. https://doi.org/10.1021/acs.chemrev.8b00395

Boyd, A. A., Flaud, P.-M., Daugey, N., & Lesclaux, R. (2003). Rate Constants for RO_2 + HO_2 Reactions Measured under a Large Excess of HO_2. *The Journal of Physical Chemistry A*, *107*(6), 818–821. https://doi.org/10.1021/jp026581r

Bunker, D. L., Garrett, B., Kleindienst, T., & Long, G. S. (1974). Discrete simulation methods in combustion kinetics. *Combustion and Flame*, *23*(3), 373–379. https://doi.org/10.1016/0010-2180(74)90120-5

Gillespie, D. T. (1976). A general method for numerically simulating the stochastic time evolution of coupled chemical reactions. *Journal of Computational Physics*, *22*(4), 403–434. https://doi.org/10.1016/0021-9991(76)90041-3

Hasan, G., Salo, V.-T., Valiev, R. R., Kubečka, J., & Kurtén, T. (2020). Comparing Reaction Routes for^{3} (RO···OR′) Intermediates Formed in Peroxy Radical Self- and Cross-Reactions. *The Journal of Physical Chemistry A*, *124*(40), 8305–8320. https://doi.org/10.1021/acs.jpca.0c05960

Hinsberg, W., & Houle, F. (2022). *Kinetiscope: A stochastic kinetics simulator, http://hinsberg.net/kinetiscope (last access: 06 Nov 2023).*

Jenkin, M. E., Valorso, R., Aumont, B., & Rickard, A. R. (2019). Estimation of rate coefficients and branching ratios for reactions of organic peroxy radicals for use in automated mechanism construction. *Atmospheric Chemistry and Physics*, *19*(11), 7691–7717. https://doi.org/10.5194/acp-19-7691-2019

Kürten, A., Rondo, L., Ehrhart, S., & Curtius, J. (2012). Calibration of a Chemical Ionization Mass Spectrometer for the Measurement of Gaseous Sulfuric Acid. *The Journal of Physical Chemistry A*, *116*(24), 6375–6386. https://doi.org/10.1021/jp212123n

Manion, J. A., Huie, R. E., Levin, R. D., Burgess Jr, D. R., Orkin, V. L., Tsang, W., McGivern, W. S., Hudgens, J. W., Knyazev, V. D., Atkinson, D. B., Chai, E., Tereza, A. M., Lin, C.-Y., Allison, T. C., Mallard, W. G., Westley, F., Herron, J. T., Hampson, R. F., & Frizzell, D. H. (2015). *NIST Chemical Kinetics Database, NIST Standard Reference Database 17, version 7.0 (web version), release 1.6.8, data version*

2015.09, National Institute of Standards and Technology, MD. https://kinetics.nist.gov/

Mellouki, A., Wallington, T. J., & Chen, J. (2015). Atmospheric Chemistry of Oxygenated Volatile Organic Compounds: Impacts on Air Quality and Climate. *Chemical Reviews*, *115*(10), 3984–4014. https://doi.org/10.1021/cr500549n

Valiev, R. R., Hasan, G., Salo, V.-T., Kubečka, J., & Kurten, T. (2019). Intersystem Crossings Drive Atmospheric Gas-Phase Dimer Formation. *The Journal of Physical Chemistry A*, *123*(30), 6596–6604. https://doi.org/10.1021/acs.jpca.9b02559

Vereecken, L., & Peeters, J. (2010). A structure–activity relationship for the rate coefficient of H-migration in substituted alkoxy radicals. *Physical Chemistry Chemical Physics*, *12*(39), 12608. https://doi.org/10.1039/c0cp00387e

Yang, X., Wang, H., Lu, K., Ma, X., Tan, Z., Long, B., Chen, X., Li, C., Zhai, T., Li, Y., Qu, K., Xia, Y., Zhang, Y., Li, X., Chen, S., Dong, H., Zeng, L., & Zhang, Y. (2024). Reactive aldehyde chemistry explains the missing source of hydroxyl radicals. *Nature Communications*, *15*(1), 1648. https://doi.org/10.1038/s41467-024-45885-w